Lawrence Berkeley National Laboratory
Recent Work

Title
Reversible disorder-order transitions in atomic crystal nucleation.

Permalink
https://escholarship.org/uc/item/9sn619tz

Journal
Science (New York, N.Y.), 371(6528)

ISSN
0036-8075

Authors
Jeon, Sungho
Heo, Taeyeong
Hwang, Sang-Yeon
et al.

Publication Date
2021

DOI
10.1126/science.aaz7555

Copyright Information
This work is made available under the terms of a Creative Commons Attribution-NonCommercial-NoDerivatives License, availalbe at
https://creativecommons.org/licenses/by-nc-nd/4.0/

Peer reviewed

eScholarship.org Powered by the California Digital Library
University of California

Reversible Disorder-Order Transitions in Atomic Crystal Nucleation

Sungho Jeon[1]†, Taeyeong Heo[1]†, Sang-Yeon Hwang[2]†‡, Jim Ciston[3], Karen C. Bustillo[3], Bryan W. Reed[4], Jimin Ham[1], Sungsu Kang[5,6], Sungin Kim[5,6], Joowon Lim[1], Kitaek Lim[1], Ji Soo Kim[5,6], Min-Ho Kang[5,6], Ruth S. Bloom[4], Sukjoon Hong[1], Kwanpyo Kim[7,8], Alex Zettl[9,10,11], Woo Youn Kim[2], Peter Ercius[3]*, Jungwon Park[5,6]*, Won Chul Lee[1]*

Affiliations:

[1]Department of Mechanical Engineering, BK21 FOUR ERICA-ACE Center, Hanyang University, Ansan, Gyeonggi 15588, Republic of Korea.

[2]Department of Chemistry, Korea Advanced Institute of Science and Technology (KAIST), Daejeon 34141, Republic of Korea.

[3]National Center for Electron Microscopy, Molecular Foundry, Lawrence Berkeley National Laboratory (LBNL), Berkeley, California 94720, United States.

[4]Integrated Dynamic Electron Solutions, Inc., Pleasanton, California 94588, United States.

[5]School of Chemical and Biological Engineering, Seoul National University, Seoul 08826, Republic of Korea.

[6]Center for Nanoparticle Research, Institute for Basic Science (IBS), Seoul 08826, Republic of Korea.

[7]Department of Physics, Yonsei University, Seoul 03722, Republic of Korea.

[8]Center for Nanomedicine, IBS, Seoul 03722, Republic of Korea.

[9]Department of Physics, University of California, Berkeley, California 94720, United States.

[10]Materials Sciences Division, LBNL, Berkeley, California 94720, United States.

[11]Kavli Energy NanoSciences Institute, Berkeley, California 94720, United States.

* Correspondence to: wonchullee@hanyang.ac.kr (W.C.L.), jungwonpark@snu.ac.kr (J.P.), or percius@lbl.gov (P.E.).

† Equally contributed authors.

‡ Present address: Samsung Advanced Institute of Technology (SAIT), Samsung Electronics, Suwon 16678, Republic of Korea.

One Sentence Summary:

In-situ electron microscopy reveals that gold atoms crystallize through dynamic and reversible processes in the early stage. (124 characters)

Abstract (123 words)**:**

Nucleation in atomic crystallization remains poorly understood despite advances in classical nucleation theory. The nucleation process has been described to involve a non-classical mechanism including a spontaneous transition from disordered to crystalline states, but a detailed understanding of dynamics requires further investigation. In-situ electron microscopy of heterogenous nucleation of individual gold nanocrystals with millisecond temporal resolution shows that the early stage of atomic crystallization proceeds through dynamic structural fluctuations between disordered and crystalline states, rather than through a single irreversible transition. Our experimental and theoretical analyses support that structural fluctuations originate from size-dependent thermodynamic stability of the two states in atomic clusters. These findings, based on dynamics in a real atomic system, reshape and improve our understanding of nucleation mechanisms in atomic crystallization.

Main Text (2,528 words)**:**

Nucleation is a critical phenomenon in the formation of many solid materials (*1-3*). Classical nucleation theory describes a pathway to crystal formation (*4, 5*), in which direct assembly of monomers occurs by density fluctuations over the surface and volume free-energy barrier. More interestingly, the nucleation process in diverse systems of colloidal particles (*6, 7*), proteins (*8, 9*), and small molecules (*10*) has shown to incorporate non-classical processes (*1*) such as a two-step nucleation mechanism (*2, 3*). In those systems, metastable intermediate clusters form and then transform to stable crystals, circumventing the high energy barrier of direct crystallization.

Atomic crystallization is affected by diverse metastable states, which inherently appear in small atomic clusters (~1 nm) with sizes equivalent to the nucleation stage (*11*). A few experimental studies have identified fully- or partially- disordered states in the early stage of atomic crystallization in solution (*12, 13*), on surfaces (*14, 15*), or in nanomaterials (*16, 17*). Due to multiple local minima with similar energy levels originating from diverse metastable states (*1, 11*), we hypothesize that the contribution of metastable states provides a dynamic nature to the early stage of crystallization. In addition, surfaces of small clusters fluctuate due to recurrent collisions of incoming atoms and desorption of surface atoms, and thus the free-energy barrier defining nuclei can be perturbed dynamically. These energetic interactions suggest that the early stage of atomic crystallization may exhibit non-classical processes governed by atomistic dynamics. Here, we investigated the heterogeneous nucleation process of gold nanocrystals on a graphene surface with atomic spatial resolution and millisecond temporal resolution.

We used three aberration-corrected TEMs (transmission electron microscope): one with a direct electron detector, the second with a scintillator-coupled camera combined with an electrostatic subframing system that further improved temporal resolution (*18*), and the third with a low-noise scintillator-coupled camera for low-dose imaging (Supplementary section 1 and fig. S1). For in-situ imaging of crystal nucleation, we prepared single-layered graphene support films on which gold(I) cyanide (AuCN) nanoribbons were synthesized (fig. S2) (*19, 20*). The electron beam acted as an imaging source as well as a reducing agent to decompose AuCN nanoribbons (about 2 – 5 nm thick) to zerovalent Au atoms and $(CN)_2$ gas (*19, 21*). The concentration of Au adatoms increased locally near the imaged nanoribbon, and the atoms aggregated to form Au nanocrystals (fig. S1A). This process occurred on the 2D (2-dimensional) surface of free-standing graphene in vacuum, minimizing electron scattering from the substrate. To investigate the process from the beginning, recording a high-speed TEM movie was synchronized with illumination of the high-intensity electron beam on a pristine sample area (fig. S1D). The advanced imaging detectors and sample geometry enabled us to achieve millisecond temporal resolution (1.6 ms and 10 ms) with atomic-scale observations.

Movie S1, with snapshots in Fig. 1A, presents a typical high-speed TEM movie (temporal resolution: 10 ms; accelerating voltage: 300 kV; current density: 7.0×10^6 A/m^2, equivalent to electron dose-rate of 4.4×10^5 e$^-$/Å^2-s) of the crystal nucleation and growth processes, whose overall characteristics are presented in the Supplementary section 2 and fig. S3. Time-resolved investigation of each nucleation path (movie S2) elucidates that the crystal nucleation proceeds through a mechanism in which an atomic cluster transforms reversibly between disordered and crystalline states many times. As shown in the first notable events of movie S2 (Fig. 1B; 7 successive frames from 140 ms to 200 ms), the first lattice fringe abruptly appears at 150 ms and disappears at 170 ms. Then, the second lattice fringe appears (190 ms) with a different lattice orientation and disappears at some point between 200 ms and 230 ms (fig. S4 and Supplementary section 3.2). From 230 ms to 1,190 ms, no lattice fringe is observed while strong fluctuations of pixel intensities in the center indicate the presence of an atomic cluster (Fig. 1D). Similar processes are repeated during the early stage of crystallization from 0 s to ~4 s (fig. S5). Short-lived lattice fringes appear and disappear repeatedly while no lattice fringe is observed in most of the frames. This phenomenon is also confirmed with multiple small peaks observed by tracking maximum intensities in 2D FFTs (fast Fourier transforms) of TEM frames over time (Fig. 1C). After ~4 s, the lattice fringe starts to grow laterally and becomes stable in the next stage of the nucleation process. Notably, this growth is not gradual, but many transitions between images that show lattice and no lattice are observed multiple times (Fig. 1, B and E). During these transitions, abrupt changes of the lattice orientations occur only when lattice fringes disappear and re-appear (Fig. 1, E and F). In the final stage (after ~5 s), a stable lattice fringe gradually grows without any further abrupt changes.

The observed lattice fringes in the TEM images indicate crystalline Au nanoparticles (fig. S11). The 2D projected areas covered by lattice fringes mostly have non-circular and irregular shapes (Fig. 1B), implying that the early-stage crystalline nuclei have non-equilibrium geometries (*16*). The frequent disappearances of existing lattice fringes, a distinguishing observation in this study, can be interpreted as a transformation of crystalline atomic structures to a disordered state. This analysis is derived from previous works which identified fluctuating disordered (*22, 23*) or quasi-melting (*24*) states of nanoclusters. TEM frames without a lattice fringe instead show continuous fluctuations of granular features whose sizes are commensurate with that of Au atoms (Fig. 1D, fig. S10, and movie S2, 0.23 s to 1.19 s), and similar series of TEM frames were presented as evidence of previous identifications of disordered states (*22-24*). Previous XRD (x-ray diffraction) analyses confirmed disordered atomic structures of small Au nanoparticles (< ~2 nm) (*25*). The presence of disordered atomic clusters in our case is also supported by Fig. 1, E and F, which show that lattice orientations abruptly changed only after they disappear and re-emerge. We can rule out other explanations for the lattice disappearance (Supplementary section 3.1), such as tilting of nanocrystals away from low-index zone axes or fast rotation of nanocrystals within our exposure time (~10 ms). Small nanocrystals (< ~2 nm) always present lattice fringes in high-resolution TEM images regardless of viewing orientations (*22, 26*), confirmed by TEM image simulations (fig. S12). The fast rotation of a nanocrystal inherently changes lattice orientations (fig. S13), but our TEM movies show that lattice orientations are fixed in successive frames during which crystalline domains decrease in size and then disappear (fig. S14).

Based on the above analysis, the process shown in Fig. 1 can be described as a trajectory of recurrent structural transformations between disordered (labeled D) and crystalline (labeled C) states, which is nucleation path #1 in Fig. 2A. In the early stage, a gold nanocluster is mostly in the disordered state and fluctuates continuously, while a few short-lived crystalline states appear with a relatively short lifetime. Repeated transformations between the two states are observed for an extended period, and ultimately a stable crystalline particle is formed. Slowing down the effective frame rate of movie S1 with frame-averaging to the previously achievable level of conventional TEM (fig. S3; 0.5 s per frame) greatly improves the signal-to-noise ratio of each TEM image, but the frame-averaged movie incorrectly suggests the process follows a sequence of irreversible steps: A blurry or granular spot forms at the nucleation site (0.5 – 1.0 s), then the spot transforms into a lattice fringe (4.5 – 5.0 s), and the lattice fringe gradually grows. However, our high-speed in-situ observations reveal that the process includes dynamic and reversible transformations between the two states.

The characteristics discovered in Fig. 1 are consistently observed in all nucleation paths investigated in this study (figs. S15 to S29 and movie S3 to S5). We modified the electron beam conditions (fig. S15) to control kinetic factors and affect the nucleation process. For example, the rate of Au adatom supply determined by radiolysis of AuCN was found to be sensitive to accelerating voltage and current density. Radiolysis of AuCN was highest at 80 kV and decreased with lower current densities (fig. S30 and Supplementary section 4.2). We performed in-situ imaging under seven different conditions (fig. S15) with accelerating voltages of either 80 kV, 200 kV, or 300 kV and current densities ranging from 6.6×10^2 A/m^2 (41 e$^-$/Å^2-s) to 6.1×10^7 A/m^2 (3.8×10^6 e$^-$/Å^2-s). The best temporal resolution achieved was 1.6 ms (at 200 kV and 6.1×10^7 A/m^2) using a subframing system (figs. S1C and S25). Thus, we investigated nucleation paths in a wide range of the averaged growth rate of Au nanoclusters from ~0.5 atoms/sec (at 200 kV and 6.6×10^2 A/m^2) to ~50 atoms/sec (at 80 kV and 5.9×10^5 A/m^2; at 200 kV and 6.1×10^7 A/m^2). Regardless of the different conditions, the existence of dynamic structural fluctuations during the nucleation process is confirmed in all 68 nucleation paths, as shown in the nucleation paths under three representative conditions in Fig. 2, A to C. In addition, structural fluctuations of neighboring nanoclusters occur asynchronously in each of the in-situ movies, and these phenomena are consistently observed under significantly different conditions (Fig. 2, D and E). It further supports that stochastic structural fluctuations are universal in the observed nucleation process (Supplementary section 4.4).

Using the multiple nucleation paths presented in Fig. 2, A to C, we performed a statistical analysis for the relative population between the disordered and crystalline states, which is indicative of the relative stability of the two states. For example, from the 20 nucleation paths in Fig. 2A and fig. S22, we calculated temporal fractions of the crystalline state (fig. S31) and investigated their relation to the sizes of nanocrystals (magenta dots in Fig. 3A). The other two cases (Fig. 2, B and C) whose current density is 10^{-3} times that of the first case were also analyzed with the identical method (orange triangles and green squares in Fig. 3A). The results from different conditions follow a similar trend, and the difference is relatively small as seen in the scattering of the data points. In all three cases, a nascent small nanocluster has a high probability of retaining the disordered state (top part in Fig. 3B). Then, the relative population of the crystalline state increases while the nanocluster grows from ~1.0 nm^2 to ~3.0 nm^2 (middle part in Fig. 3B; equivalent circular diameters: ~1.1 nm – ~2.0 nm). Eventually, the enlarged nanocluster maintains the crystalline state (bottom part in Fig. 3B). This implies that the observed process is an evolution of atomic structures through stochastic and dynamic fluctuations between two states whose relative stability is size-dependent. Figure 3A also indicates that the observed structural fluctuations are mainly directed by formation and early-stage growth of nanoclusters and are not an artifact induced by the electron beam. The electron beam can transfer a certain amount of energy to Au atoms and clusters elastically and/or inelastically, which may generate the crystalline-to-disordered transformations of clusters. To confirm this was not the case in our study, sub-2 nm Au nanoclusters were prepared by a typical colloidal synthesis and observed under the same imaging condition for a prolonged time (Supplementary section 4.1). Small-sized pre-synthesized clusters occasionally show disordered structures (fig. S32), consistent with previous studies (*22-28*). However, Fig. 3A indicates that the pre-synthesized clusters (gray circles) were mostly in the crystalline state throughout imaging for cluster sizes > ~1 nm, clearly different from the other cases (solid symbols) observed during the nucleation process. Additional extensive discussion regarding electron beam effects is in Supplementary section 4 (figs. S15, S16, S25 to S34).

The free-energy change for the transition from disordered to crystalline states is usually negative and high enough to make the transition spontaneous. However, statistical observations of the reversible and dynamic transformations in Fig. 3, A and B, imply that the energy difference and the barrier between the two states is small when the cluster size is small in the early stage of nucleation (top part in Fig. 3B). As nanoclusters grow, the energy difference gradually increases and the nanoclusters present the crystalline state more frequently. From a certain nanocluster size (~2.0 nm in our study), nanoclusters are trapped in the crystalline state due to the increased energy difference (bottom part in Fig. 3B). Many theoretical and experimental studies (*22-28*) have reported that small (< ~2 nm) nanoparticles can have disordered atomic structures even in ambient conditions. Melting point depression (*29-31*) also means that crystalline-to-disordered transitions require significantly reduced energy in small nanoparticles compared to bulk materials. These previous results consistently support the low energy barrier of the crystalline-to-disordered transformation of small nanoclusters. Fluctuations between two states over a free-energy barrier are a key thermodynamic concept of classical nucleation theory. Although this concept is not excluded in the framework of non-classical two-step nucleation (fig. S35) (*2*), only a few studies (*7, 17, 32*) have investigated it. The above thermodynamic description and our high-speed observations reintroduce as well as verify that reversible and dynamic transformations can occur in non-classical nucleation pathways.

The low energy barrier of the crystalline-to-disordered transformation can be overcome by various sources. Monomer attachment is an exergonic reaction and can deposit a relatively large amount of energy to nascent nanoclusters as thermal fluctuations and the electron beam. We performed first-principles calculations of the energy released from binding reactions between an Au atom and hemispheroidal Au nanocrystals (Fig. 3C, figs. S36 and S37, tables S1 to S3, and Supplementary section 5), and evaluated whether the calculated energies are comparable to collapsing crystalline structures by using thermal energies required to increase temperatures of the nanocrystals to the depressed melting points (*29-31*). The crossover of the two energies occurs at the nanocrystal size containing 49 constituent atoms (nanocrystal area: ~1.4 nm^2) in Fig. 3C. This implies that recurrent binding of Au atoms can provide sufficient energy to small clusters to drive toward the disordered state. Experimental results that partly support this hypothesis are presented in Fig.3, D to F, fig. S38, and movie S6, which show that the binding of a small atomic cluster (composed of ~10 atoms, ~0.7 nm^2) to a large nanocrystal induces noticeable structural transformations to the disordered state. Just after the atomic-cluster binding, the crystalline area is gradually reduced and then recovered (~9.0 nm^2 → ~3.0 nm^2 → ~10.0 nm^2). We also found that coalescence of small nanocrystals drives either or both of the nanocrystals to visit the disordered state (figs. S39 to S43 and movie S7). Therefore, reversible transformations commonly occur throughout various stages in our model system. Obviously, our system does not universally reproduce the entire scope of crystal nucleation starting from scattered monomers. However, our study reveals near-atomic scale dynamics from concentrated adatoms to the formation of a stable crystal, thus addressing a critical step that determines the nucleation pathway in many different types of crystallization processes (Supplementary section 6 and fig. S44).

In this study, we found that crystal nucleation of gold clusters on graphene progresses through reversible structural fluctuations between disordered and crystalline states. High-speed in-situ observations of a real atomic system confirm non-classical and dynamic natures of the nucleation process during atomic crystallization. Our findings clarify fundamental mechanisms underlying the nucleation stage of material growth including thin-film deposition, interface-induced precipitation, and nanoparticle formation.

References and Notes:

1. J. J. De Yoreo *et al.*, Crystallization by particle attachment in synthetic, biogenic, and geologic environments. *Science* **349**, 498 (2015).
2. P. G. Vekilov, Nucleation. *Cryst. Growth Des.* **10**, 5007-5019 (2010).
3. D. Erdemir, A. Y. Lee, A. S. Myerson, Nucleation of crystals from solution: Classical and two-step models. *Acc. Chem. Res.* **42**, 621-629 (2009).
4. J. J. Chen *et al.*, Building two-dimensional materials one row at a time: Avoiding the nucleation barrier. *Science* **362**, 1135-1139 (2018).
5. M. Sleutel, J. Lutsko, A. E. S. Van Driessche, M. A. Duran-Olivencia, D. Maes, Observing classical nucleation theory at work by monitoring phase transitions with molecular precision. *Nat. Commun.* **5**, 5598 (2014).
6. Z. H. Ou, Z. W. Wang, B. B. Luo, E. Luijten, Q. Chen, Kinetic pathways of crystallization at the nanoscale. *Nat. Mater.* **19**, 450-455 (2020).
7. T. H. Zhang, X. Y. Liu, Nucleation: What happens at the initial stage? *Angew. Chem. Int. Ed.* **48**, 1308-1312 (2009).
8. P. R. tenWolde, D. Frenkel, Enhancement of protein crystal nucleation by critical density fluctuations. *Science* **277**, 1975-1978 (1997).
9. L. Houben, H. Weissman, S. G. Wolf, B. Rybtchinski, A mechanism of ferritin crystallization revealed by cryo-STEM tomography. *Nature* **579**, 540-543 (2020).
10. M. H. Nielsen, S. Aloni, J. J. De Yoreo, In situ TEM imaging of CaCO3 nucleation reveals coexistence of direct and indirect pathways. *Science* **345**, 1158-1162 (2014).
11. A. S. Barnard, N. P. Young, A. I. Kirkland, M. A. van Huis, H. F. Xu, Nanogold: A quantitative phase map. *ACS Nano* **3**, 1431-1436 (2009).
12. N. D. Loh *et al.*, Multistep nucleation of nanocrystals in aqueous solution. *Nat. Chem.* **9**, 77-82 (2017).
13. J. Yang *et al.*, Amorphous-phase-mediated crystallization of Ni nanocrystals revealed by high-resolution liquid-phase electron microscopy. *J. Am. Chem. Soc.* **141**, 763-768 (2019).
14. M. H. Hu, S. Noda, H. Komiyama, Amorphous-to-crystalline transition during the early stages of thin film growth of Cr on SiO2. *J. Appl. Phys.* **93**, 9336-9344 (2003).
15. L. Fei *et al.*, Observable two-step nucleation mechanism in solid-state formation of tungsten carbide. *ACS Nano* **13**, 681-688 (2019).
16. J. H. Zhou *et al.*, Observing crystal nucleation in four dimensions using atomic electron tomography. *Nature* **570**, 500-503 (2019).
17. K. C. Cao *et al.*, Atomic mechanism of metal crystal nucleus formation in a single-walled carbon nanotube. *Nat. Chem.* **12**, 9 (2020).
18. B. W. Reed *et al.*, Electrostatic subframing and compressive-sensing video in transmission electron microscopy. *Struct. Dynam.* **6**, 054303 (2019).
19. W. C. Lee *et al.*, Graphene-templated directional growth of an inorganic nanowire. *Nat. Nanotechnol.* **10**, 423-428 (2015).
20. J. Kim *et al.*, Precise identification of graphene's crystal structures by removable nanowire epitaxy. *J. Phys. Chem. Lett.* **8**, 1302-1309 (2017).
21. M. T. Beck *et al.*, Gold nano-particle formation from crystalline AuCN: Comparison of thermal, plasma- and ion-beam activated decomposition. *J. Solid State Chem.* **246**, 65-74 (2017).
22. Z. W. Wang, R. E. Palmer, Experimental evidence for fluctuating, chiral-type Au-55 clusters by direct atomic imaging. *Nano Lett.* **12**, 5510-5514 (2012).

23. T. J. Pennycook, J. R. McBride, S. J. Rosenthal, S. J. Pennycook, S. T. Pantelides, Dynamic fluctuations in ultrasmall nanocrystals induce white light emission. *Nano Lett.* **12**, 3038-3042 (2012).
24. P. M. Ajayan, L. D. Marks, Experimental evidence for quasimelting in small particles. *Phys. Rev. Lett.* **63**, 279-282 (1989).
25. V. Petkov *et al.*, Periodicity and atomic ordering in nanosized particles of crystals. *J. Phys. Chem. C* **112**, 8907-8911 (2008).
26. L. Li *et al.*, Noncrystalline-to-crystalline transformations in Pt nanoparticles. *J. Am. Chem. Soc.* **135**, 13062-13072 (2013).
27. Y. Sun, L. Zhuang, J. Lu, X. Hong, P. Liu, Collapse in crystalline structure and decline in catalytic activity of Pt nanoparticles on reducing particle size to 1 nm. *J. Am. Chem. Soc.* **129**, 15465-15467 (2007).
28. I. L. Garzon *et al.*, Lowest energy structures of gold nanoclusters. *Phys. Rev. Lett.* **81**, 1600-1603 (1998).
29. P. Buffat, J. P. Borel, Size effect on melting temperature of gold particles. *Phys. Rev. A* **13**, 2287-2298 (1976).
30. K. Dick, T. Dhanasekaran, Z. Y. Zhang, D. Meisel, Size-dependent melting of silica-encapsulated gold nanoparticles. *J. Am. Chem. Soc.* **124**, 2312-2317 (2002).
31. W. H. Qi, M. P. Wang, Size and shape dependent melting temperature of metallic nanoparticles. *Mater. Chem. Phys.* **88**, 280-284 (2004).
32. P. W. Sutter, E. A. Sutter, Dispensing and surface-induced crystallization of zeptolitre liquid metal-alloy drops. *Nat. Mater.* **6**, 363-366 (2007).

-- References cited in Supplementary Materials --

33. W. Regan *et al.*, A direct transfer of layer-area graphene. *Appl. Phys. Lett.* **96**, 113102 (2010).
34. M. Azubel *et al.*, Electron microscopy of gold nanoparticles at atomic resolution. *Science* **345**, 909-912 (2014).
35. M. Brust, M. Walker, D. Bethell, D. J. Schiffrin, R. Whyman, Synthesis of thiol-derivatised gold nanoparticles in a two-phase liquid–liquid system. *ChemComm*, 801-802 (1994).
36. X. Yuan *et al.*, Balancing the rate of cluster growth and etching for gram-scale synthesis of thiolate-protected Au_{25} nanoclusters with atomic precision. *Angew. Chem. Int. Ed.* **126**, 4711-4715 (2014).
37. B. W. Reed, S. T. Park, D. J. Masiel, Beyond movie mode: bridging the gap of time resolution. *Microsc. Microanal.* **22**, 706-707 (2016).
38. T. LaGrange, B. W. Reed, D. J. Masiel, Movie-mode dynamic electron microscopy. *MRS Bull.* **40**, 22-28 (2015).
39. M. J. Hytch, Analysis of variations in structure from high resolution electron microscope images by combining real space and Fourier space information. *Microsc. Microanal. Microst.* **8**, 41-57 (1997).
40. E. J. Kirkland, *Advanced computing in electron microscopy*. (Springer Science & Business Media, 2010).
41. J. A. Venables, G. D. T. Spiller, M. Hanbucken, Nucleation and growth of thin-films. *Rep. Prog. Phys.* **47**, 399-459 (1984).
42. Z. W. Wang, R. E. Palmer, "Atomic-scale structure analysis by advanced transmission electron microscopy" in *Frontiers of Nanoscience*. (Elsevier, 2015), vol. 9, chap. 6.
43. R. Egerton, Choice of operating voltage for a transmission electron microscope. *Ultramicroscopy* **145**, 85-93 (2014).
44. R. Egerton, P. Li, M. Malac, Radiation damage in the TEM and SEM. *Micron* **35**, 399-409

(2004).
45. R. Egerton, Beam-induced motion of adatoms in the transmission electron microscope. *Microsc. Microanal.* **19**, 479 (2013).
46. T. Gerber, C. Busse, J. Mysliveček, J. Coraux, T. Michely, A versatile fabrication method for cluster superlattices. *New J. Phys.* **11**, 103045 (2009).
47. I. Gonzalez-Martinez *et al.*, Electron-beam induced synthesis of nanostructures: a review. *Nanoscale* **8**, 11340-11362 (2016).
48. O. Dyck *et al.*, Atom-by-atom fabrication with electron beams. *Nat. Rev. Mater.* **4**, 497-507 (2019).
49. B. H. Kim *et al.*, Liquid-phase transmission electron microscopy for studying colloidal inorganic nanoparticles. *Adv. Mater.* **30**, 1703316 (2018).
50. D. Schebarchov, F. Baletto, D. Wales, Structure, thermodynamics, and rearrangement mechanisms in gold clusters—insights from the energy landscapes framework. *Nanoscale* **10**, 2004-2016 (2018).
51. G. Te Velde, E. Baerends, Precise density-functional method for periodic structures. *Phys. Rev. B: Condens. Matter* **44**, 7888 (1991).
52. G. te Velde *et al.*, Chemistry with ADF. *J. Comput. Chem.* **22**, 931-967 (2001).
53. J. P. Perdew, K. Burke, M. Ernzerhof, Generalized gradient approximation made simple. *Phys. Rev. Lett.* **77**, 3865-3868 (1996).
54. S. Grimme, S. Ehrlich, L. Goerigk, Effect of the damping function in dispersion corrected density functional theory. *J. Comput. Chem.* **32**, 1456-1465 (2011).
55. E. Vanlenthe, E. J. Baerends, J. G. Snijders, Relavistic total-energy using regular approximations. *J. Chem. Phys.* **101**, 9783-9792 (1994).
56. P. H. T. Philipsen, E. vanLenthe, J. G. Snijders, E. J. Baerends, Relativistic calculations on the adsorption of CO on the (111) surfaces of Ni, Pd, and Pt within the zeroth-order regular approximation. *Phys. Rev. B: Condens. Matter* **56**, 13556-13562 (1997).
57. K. Dick, T. Dhanasekaran, Z. Zhang, D. Meisel, Size-dependent melting of silica-encapsulated gold nanoparticles. *J. Am. Chem. Soc.* **124**, 2312-2317 (2002).
58. D. A. McQuarrie, J. D. Simon, *Physical Chemistry: a Molecular Approach*. Sausalito: University Science Books (University Science Books, Sausalito, CA, 1997).
59. M. Schwartzkopf *et al.*, From atoms to layers: in situ gold cluster growth kinetics during sputter deposition. *Nanoscale* **5**, 5053-5062 (2013).
60. P. Puri, V. Yang, Effect of particle size on melting of aluminum at nano scales. *J. Phys. Chem. C* **111**, 11776-11783 (2007).
61. J. van Embden, A. S. Chesman, J. J. Jasieniak, The heat-up synthesis of colloidal nanocrystals. *Chem. Mater.* **27**, 2246-2285 (2015).
62. H. Stanley, Introduction to Phase Transitions and Critical Phenomena Oxford Univ. *Press, New York*, (1987).
63. M. Challa, D. Landau, K. Binder, Monte Carlo studies of finite-size effects at first-order transitions. *Phase Transit.* **24**, 343-369 (1990).
64. H. Zheng *et al.*, Observation of transient structural-transformation dynamics in a Cu2S nanorod. *Science* **333**, 206-209 (2011).
65. P. G. Vekilov, The two-step mechanism of nucleation of crystals in solution. *Nanoscale* **2**, 2346-2357 (2010).
66. P. G. Vekilov, Dense liquid precursor for the nucleation of ordered solid phases from solution. *Cryst. Growth Des.* **4**, 671-685 (2004).

Acknowledgments: The authors thank Andrew Minor, Taeghwan Hyeon, Shoji Takeuchi, and Sungwook Chung for helpful discussions. **Funding:** This work was mainly supported by the National Research Foundation of Korea (NRF) funded by the Ministry of Science and ICT (MSIT) and the Ministry of Education (MOE) under Contract No. 2016R1C1B1014940 and 2019R1F1A1059099. Work at the Molecular Foundry was supported by the Office of Science, Office of Basic Energy Sciences, of the U.S. Department of Energy under Contract No. DE-AC02-05CH11231. The authors also acknowledge multiple financial supports from: Institutes for Basic Science (IBS-R006-D1); NRF funded by the Korea government (MSIT and MOE) under Contract No. 2017R1C1B2010434, 2017R1A5 A1015365, 2019M3E6A1064877, 2018R1A5A1025208, 2017R1A5A1014862, 2015M3C1B2052811, 2018R1D1A1B07050575, and 2020R1F1A1065856; Samsung Science and Technology Foundation for developing the data analysis and TEM simulation methods (M.-H.K. and J.P., SSTF-BA1802-08); U.S. Department of Energy, Office of Science, Office of Basic Energy Sciences, Materials Sciences and Engineering Division (DE-AC02-05-CH11231) within the Nanomachines Programs (KC1203) which supported preliminary TEM measurements; U.S. National Science Foundation (DMR-1807233) which provided for development of graphene TEM supports. **Author contributions:** S.J., T.H., and S.-Y.H. contributed equally to this work. W.C.L., J.P, and P.E. conceived the design of the study. S.J., S. K., J.C., K.C.B., B.W.R., R.S.B., P.E., and W.C.L. performed in-situ TEM imaging. S.J. and T.H. analyzed the data. S.-Y.H. and W.Y.K. performed first-principles calculations. J.S.K., J.H., S.K., J.L., K.L., M.-H.K., S.H., K.K., and A.Z. contributed to sample preparation or data analysis. S.J., T.H., S.-Y.H., J.C., K.C.B., B.W.R., S.H., P.E., J.P., and W.C.L. wrote the manuscript. All authors discussed the results and commented on the manuscript.; **Competing interests:** The authors declare no competing interests. **Data and materials availability:** All data are available in the main text or the supplementary materials.

Supplementary Materials:

Materials and Methods (Supplementary section 1)

Supplementary Text (Supplementary sections 2 to 6)

Figures S1-S44

Tables S1-S3

Movies S1-S7

References (*33-66*)

Figure captions:

Fig. 1. Direct observation of formation of an Au nanocrystal. (**A**) TEM image frames from the high-speed *in-situ* movie (movie S1). Scale bar: 5 nm. Au nanocrystals in the final image are marked with red circles. (**B**) Individual frames from movie S2 showing a nucleation process (yellow box in (A), temporal resolution: 10 ms). Lower left: atomic model of the nanocrystal. Red dashed lines indicate nanocrystal <111> directions. Lower right: FFT (Fast Fourier Transform) image. Scale bar: 1 nm. The areas of Au lattices and AuCN nanowires are pseudo-colored in red and light-green, respectively. Blue circles indicate nanoclusters in the disordered state, and purple circles indicate the undefinable state (the crystalline/disordered classification is unclear). (**C**) Maximum intensity of the FFT image as a function of time. The signals from a graphene area represent ground noise levels (negative control) of this analysis. (**D**) A color map obtained from standard deviations of intensities from 230 ms to 1,190 ms for each pixel. Scale bar: 1 nm. (**E**) Nanocrystal area from 4.00 s to 5.50 s. (**F**) Direction of <111> lattices from 4.00 s to 5.50 s. Vertical dotted lines in (E) and (F) correspond to the time-labeled images in (B). Related images and detailed methods are presented in figs. S3 to S10.

Fig. 2. Multiple nucleation paths of Au nanocrystals. (**A** to **C**) Trajectories of structural transitions between disordered and crystalline states in multiple nucleation paths observed at 300 kV and 7.0×10^6 A/m^2 (A), at 200 kV and 5.6×10^3 A/m^2 (B), and at 80 kV and 5.6×10^3 A/m^2 (C). Red and blue shadings are visual guides for indicating crystalline (labeled C) and disordered (labeled D) states, respectively. The nucleation path #1 in (A) is the data set in Fig. 1. (**D** and **E**) TEM images and trajectories of structural transitions showing asynchronized structural fluctuations of two neighboring nanoclusters observed at 300 kV and 7.0×10^6 A/m^2 (D) and at 200 kV and 6.6×10^2 A/m^2 (E). The two cases have 4 orders of magnitude difference in current density. Scale bars: 1nm.

Fig. 3. Experimental and theoretical investigations of the crystalline-to-disordered transformations during the nucleation process. (**A**) Temporal fraction of crystalline states versus 2D projected area of Au nanocrystals observed during the nucleation processes (solid symbols) and observed using pre-synthesized Au nanoclusters (gray circles). The dashed curves represent fitting lines to the data with sigmoid (logistic) functions. (**B**) Size-dependent characteristics of nanoclusters during the nucleation process. Left: Schematic energy diagrams showing the nucleation mechanisms of nanocrystals from small (i) to large (iii) sizes. Right: Histograms of the temporal fractions of crystalline states for three size-ranges (0 – 1.0 nm^2, 1.0 – 3.0 nm^2, and 3.0 – 6.0 nm^2) and three different imaging conditions indicated in (A). (**C**) First-principles calculations of the binding energy between an Au atom and hemispheroidal Au_n nanocrystals. The binding energy is compared to energy required to reach the melting point of Au_{n+1} nanocrystals. Inset: Binding model at n = 37. (**D**) Sequential TEM images showing the binding of a small nanocluster (colored in blue) to a large nanocrystal (colored in red). Insets: FFT images of the nanocrystal. (**E**) Time-labeled contour plots of crystalline areas during partial collapse (left) and re-crystallization (right). (**F**) Maximum intensities of the FFT images. Vertical dotted lines and axes in (F) correspond to the time-labeled images in (D), respectively. Scale bars: 1 nm.

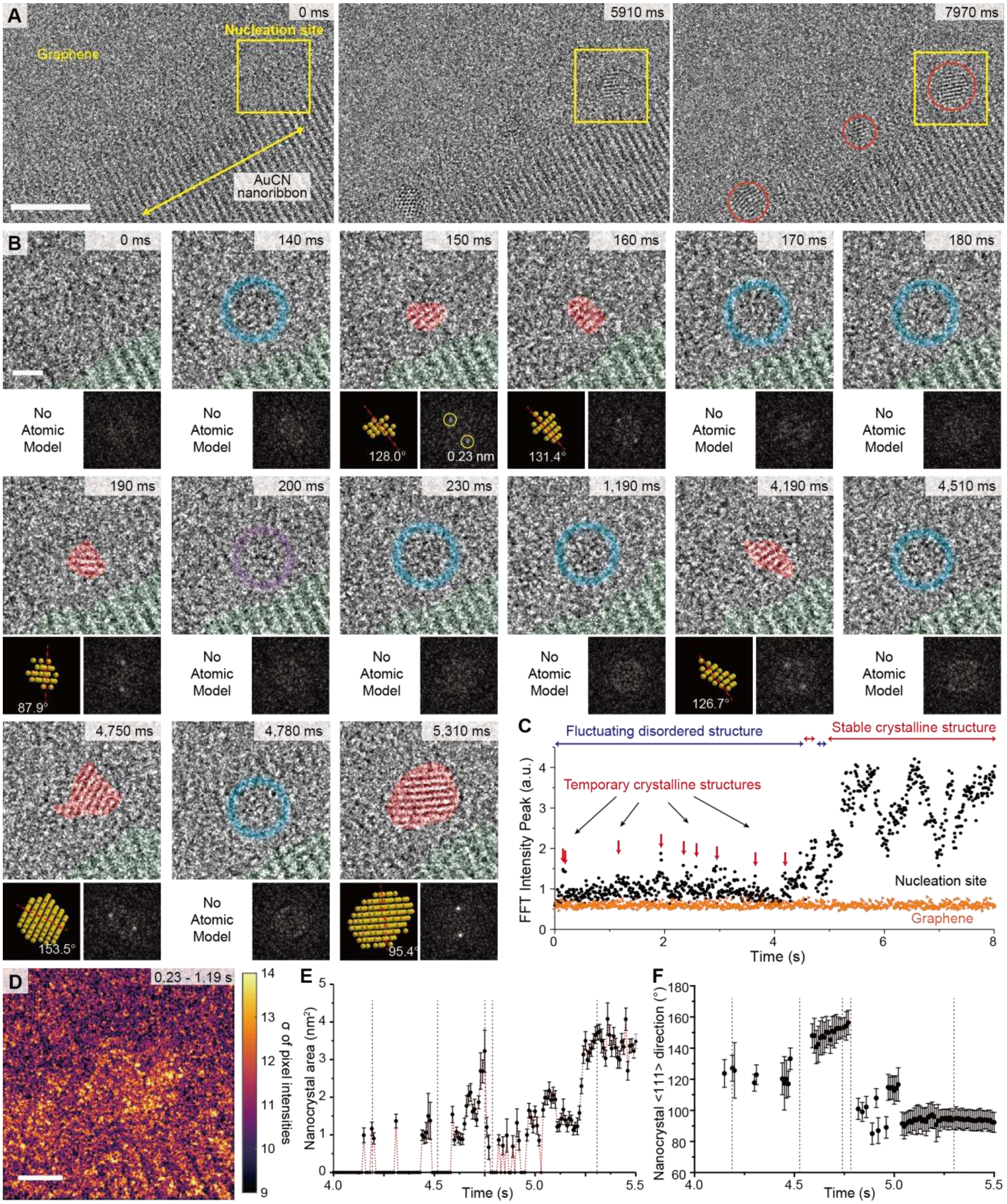
A
0 ms
Nucleation site
Graphene
AuCN nanoribbon
5910 ms
7970 ms
B
0 ms
140 ms
150 ms
160 ms
170 ms
180 ms
No Atomic Model
128.0°
0.23 nm
131.4°
190 ms
200 ms
230 ms
1,190 ms
4,190 ms
4,510 ms
87.9°
126.7°
4,750 ms
4,780 ms
5,310 ms
153.5°
95.4°
C
Fluctuating disordered structure
Stable crystalline structure
Temporary crystalline structures
FFT Intensity Peak (a.u.)
Nucleation site
Graphene
Time (s)
0
2
4
6
8
1
3
D
0.23 - 1.19 s
σ of pixel intensities
9
10
11
12
13
14
E
Nanocrystal area (nm^2)
Time (s)
4.0
4.5
5.0
5.5
5
F
Nanocrystal <111> direction (°)
60
80
100
120
140
160
180
Time (s)

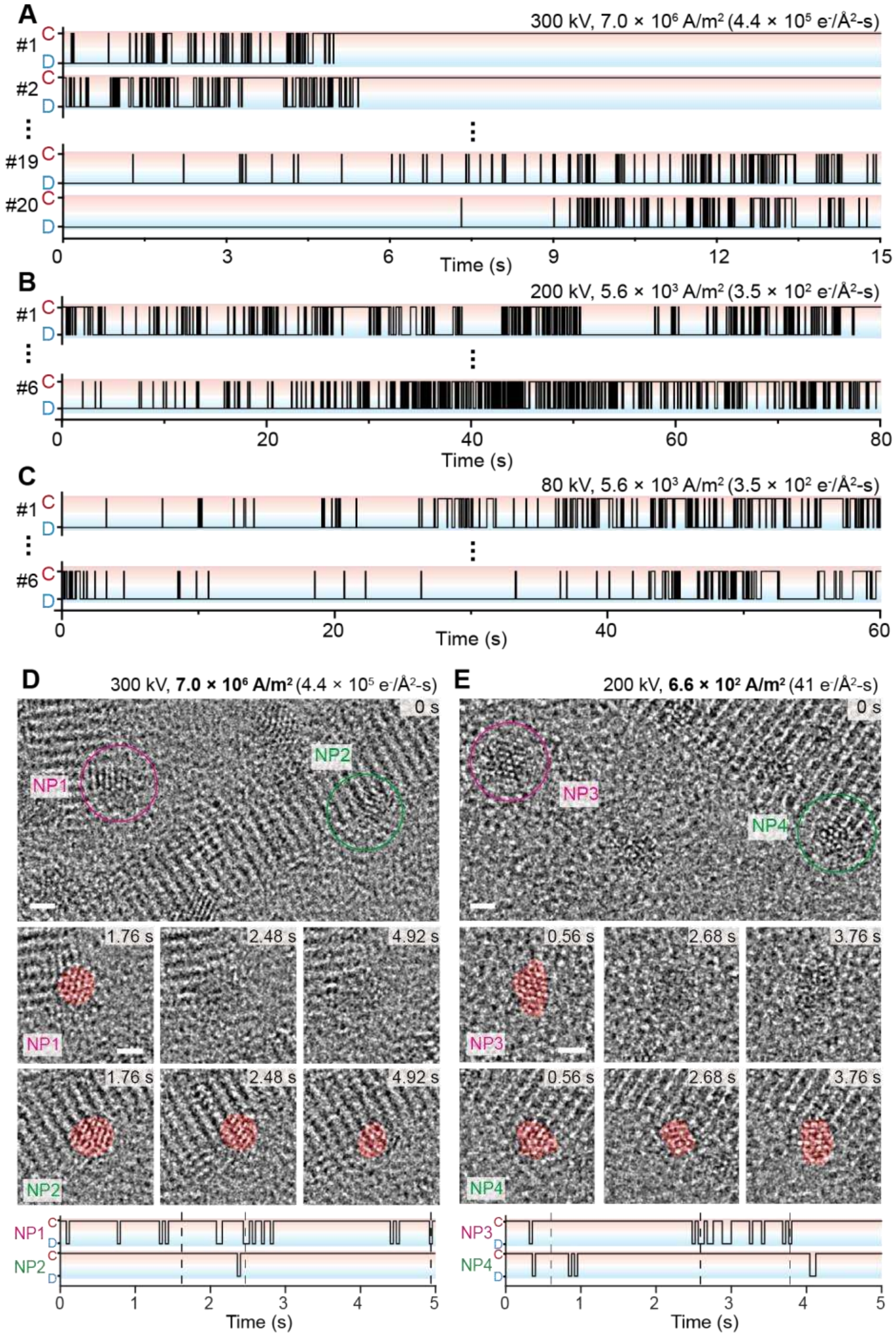
A
300 kV, 7.0 × 10⁶ A/m² (4.4 × 10⁵ e⁻/Å²-s)
#1
#2
#19
#20
C
D
0
3
6
9
12
15
Time (s)
B
200 kV, 5.6 × 10³ A/m² (3.5 × 10² e⁻/Å²-s)
#1
#6
0
20
40
60
80
Time (s)
C
80 kV, 5.6 × 10³ A/m² (3.5 × 10² e⁻/Å²-s)
#1
#6
0
20
40
60
Time (s)
D
300 kV, 7.0 × 10⁶ A/m² (4.4 × 10⁵ e⁻/Å²-s)
0 s
NP1
NP2
1.76 s
2.48 s
4.92 s
E
200 kV, 6.6 × 10² A/m² (41 e⁻/Å²-s)
0 s
NP3
NP4
0.56 s
2.68 s
3.76 s
0
1
2
3
4
5
Time (s)

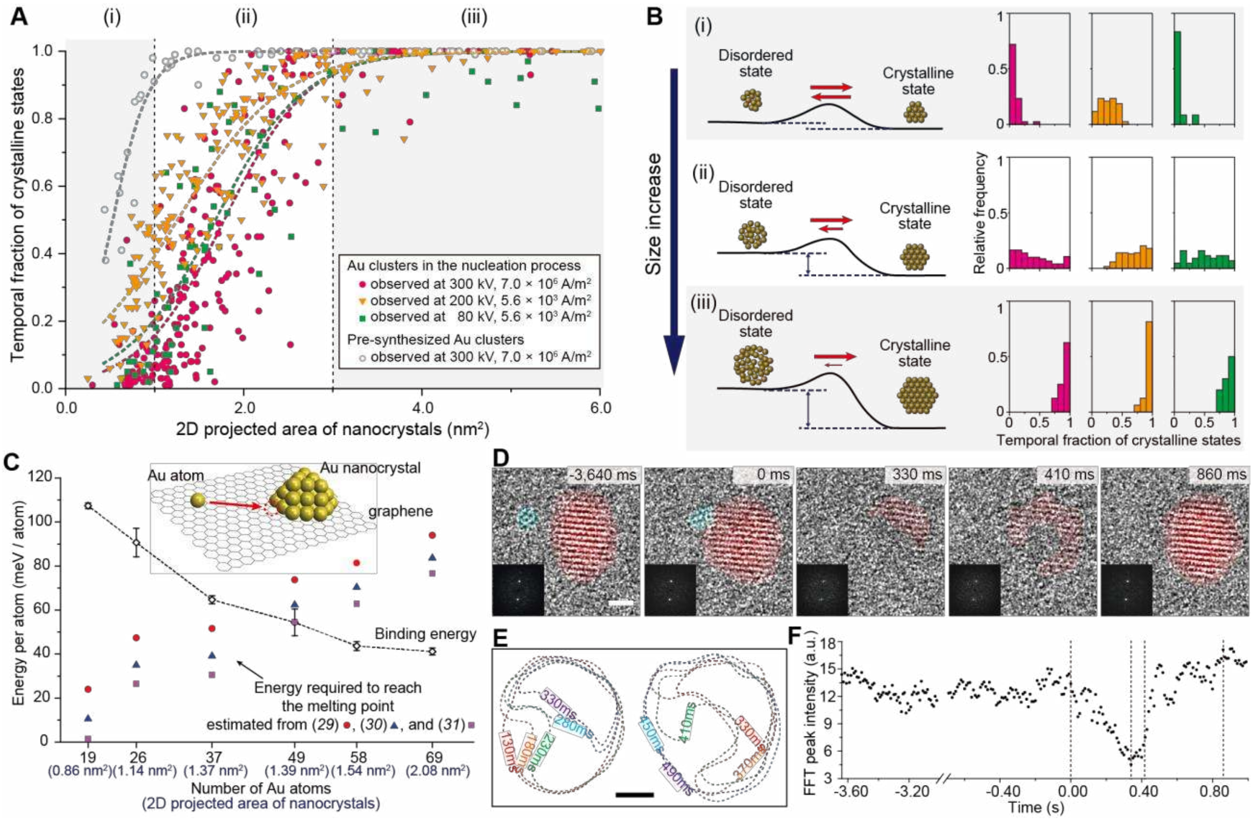
A
(i)
(ii)
(iii)
Temporal fraction of crystalline states
2D projected area of nanocrystals (nm²)
Au clusters in the nucleation process
observed at 300 kV, 7.0 × 10⁶ A/m²
observed at 200 kV, 5.6 × 10³ A/m²
observed at 80 kV, 5.6 × 10³ A/m²
Pre-synthesized Au clusters
observed at 300 kV, 7.0 × 10⁶ A/m²
B
Size increase
Disordered state
Crystalline state
Relative frequency
Temporal fraction of crystalline states
C
Au atom
Au nanocrystal
graphene
Energy per atom (meV / atom)
Binding energy
Energy required to reach the melting point estimated from (29), (30), and (31)
Number of Au atoms
(2D projected area of nanocrystals)
19 (0.86 nm²)
26 (1.14 nm²)
37 (1.37 nm²)
49 (1.39 nm²)
58 (1.54 nm²)
69 (2.08 nm²)
D
-3,640 ms
0 ms
330 ms
410 ms
860 ms
E
130ms
180ms
230ms
280ms
330ms
370ms
410ms
450ms
490ms
F
FFT peak intensity (a.u.)
Time (s)